CHINESE OPTICS LETTERS

Vol. 21, No. 10 | October 2023

Nanometer-scale displacement measurement based on an orthogonal dual Michelson interferometer

Ju Wang (王 菊), Ziheng Cai (蔡滋恒), Jinlong Yu (于晋龙)*, Hao Luo (罗 浩), and Chuang Ma (马 闯)

School of Electrical and Information Engineering, Tianjin University, Tianjin 300072, China

*Corresponding author: yujinlong@tju.edu.cn

Received March 10, 2023 | Accepted May 11, 2023 | Posted Online August 18, 2023

In this Letter, we propose a simple structure of an orthogonal type double Michelson interferometer. The orthogonal detection method overcomes the problems of uneven ranging sensitivity and the inability of traditional interferometers to determine the displacement direction. The displacement measurement principle and signal processing method of the orthogonal double interferometer are studied. Unlike the arctangent algorithm, the displacement analysis uses the arc cosine algorithm, avoiding any pole limit in the distance analysis process. The minimum step size of the final experimental displacement system is 5 nm, which exhibits good repeatability, and the average error is less than 0.12 nm.

Keywords: orthogonal detection; nanoscale displacement measurement; laser interferometer.

DOI: 10.3788/COL202321.101201

1. Introduction

Since the beginning of the 21st century, with the rapid development of microelectronics manufacturing, ultraprecision machining, aerospace, and other fields, high-precision and high-sensitivity microdisplacement measurements have received significant attention[1–3]. Currently, these measurement techniques are roughly divided into two categories: nonoptical and optical methods. Nonoptical methods include capacitive and inductive sensors[4–6]. Although these methods can achieve high-resolution, high-precision, and low-power microdisplacement measurements, their measurement range is only from tens of nanometers to micrometers[7]. In contrast, optical methods, including grating interferometry and laser interferometry[8–11], are widely used in microdisplacement measurements owing to their laser monochromaticity and good coherence[12,13]. The most advanced lithography machine, produced by advanced semiconductor material lithography (ASML), uses two-dimensional grating measurement technology. The grating displacement measurement is based on the grating pitch, which has low sensitivity to the external environment, and the repeated positioning accuracy can reach several nanometers[14]. However, in the grating production process, an ultraprecise laser interferometer is still required for positioning and motion locking[15]. Therefore, in modern ultraprecision processing, laser interferometry is widely used, owing to its advantages of traceability, high measurement accuracy, fast response time, and being noncontact.

The Michelson interferometer is the most typical laser interferometer. The measurement beam is reflected by the target and interferes with the reference beam, and the intensity of the interference signal varies periodically according to $\lambda/2$. Although it can achieve nanometer-level measurement accuracy, only a one-way output signal of light intensity can lead to nonlinear changes with the change in the distance. This may result in uneven ranging sensitivity and the inability to judge the direction of target displacement. To solve the above problems, researchers have conducted considerable improvement work on traditional interferometers.

Chu *et al.*[16] proposed a signal subdivision method that can be used in laser interferometers. The combination of a double threshold method and tangent subdivision method overcomes the inconsistency in the sensitivity of the ratio-amplitude subdivision method within a signal period. However, the signal-to-noise ratio of the fringe signal directly determines the signal subdivision accuracy, thus limiting system performance. Xu *et al.*[17] designed a nanopositioning system using a polarization laser interferometer. The photoelectric sensor of the traditional single-frequency laser interferometer is replaced by a polarimeter and equipped with polarization beam-splitting elements, polarizers, etc. The displacement is converted into the rotation angle of the synthesized light in the vibration direction using the interference optical path, and the discrimination of the displacement direction is realized. The minimum step size of the system reaches 5 nm. When building the single-frequency polarization laser interferometer, the polarizer requires strict adjustment at 45° in both directions; otherwise, phase errors will be introduced[18], and the intensity noise generated by the laser spontaneous radiation will also affect the interferometric system[19]. The use of phase compensation and orthogonal

© 2023 Chinese Optics Letters

detection technology can effectively reduce the impact of nonideal system construction and laser intensity noise[20–22] and improve the measurement accuracy and stability of laser interferometers. Cui *et al.*[23] studied a novel single-frequency laser interferometer for nanometer measurement and constructed a four-way quadrature detection structure. They also eliminated the polarization mixing cross talk with the minimum number of quadrature phase error sources and reduced the interferometer period nonlinearity error to 0.2 nm by offset correction. However, the arctangent algorithm in the phase resolution process is restricted by the pole limitation. Therefore, the signal amplitude carrying phase information needs to be quantized, sampled, and electronically subdivided to obtain the phase change, and the electronic subdivision accuracy limits the system resolution.

In this study, taking advantage of orthogonal detection, an orthogonal dual Michelson interferometer displacement measurement system is built, wherein two mutually orthogonal output signals are used to distinguish the displacement direction. This solves the shortcomings of the uneven ranging sensitivity of the traditional Michelson interferometer. The arc cosine algorithm is used for signal demodulation, which overcomes the problem of poles in the arctangent algorithm.

2. Experimental Setup and Principle Analysis

A schematic of the orthogonal double Michelson interferometer is shown in Fig. 1. A semiconductor laser (with a line width of 100 kHz and power stability within ±3% for more than 8 h of continuous operation) produces linearly polarized light with a wavelength λ of 1550 nm. The laser is guided to a polarization-maintaining fiber collimator (with central wavelength of 1550 nm, working distance of 300 mm, and insertion loss of 0.7 dB) through an optical fiber. The light emitted by the transmitting collimator is separated by a nonpolarizing beam splitter (NPBS, composed of two right-angle prisms, with a splitting ratio of 50:50 and insensitivity to polarization) in sequence to form a measurement beam and two reference beams. The two reference beams are reflected by reference mirrors 1 and 2 and then reach the receiving collimator through NPBSs 1 and 2.

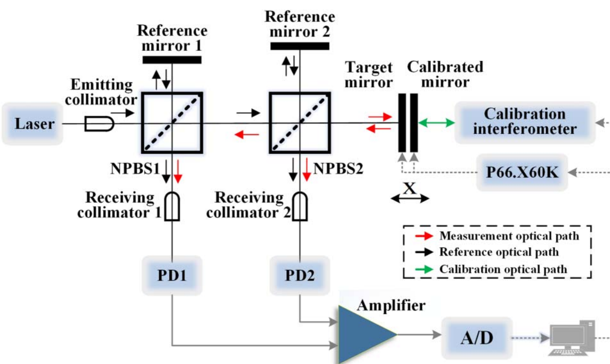

Fig. 1. Experimental setup for the orthogonal dual interferometer.

The measurement beam is reflected by the target mirror and then passes consecutively through the two NPBSs, forming two measurement beams that interfere with the two reference beams at receiving collimators 1 and 2. The receiving collimator couples the interference light into the fiber, and the photodetectors (PD1 and PD2) convert the two interference light signals in the two receiving collimators into electrical signals. The displacement of the target mirror relative to the x direction is analyzed using the interference signal after passing through the amplifier and digital to analog (A/D) module. A P66.X60K one-dimensional x direction piezoelectric nanopositioning stage (with internal high-resolution and fast-response strain sensors with closed-loop resolution of up to 2 nm) is selected to drive the target mirror.

The calibration mirror is fixed on the nanopositioning stage together with the target mirror. The picometer precision laser interferometer (Attocube Systems AG brand IDS3010, with strong ranging capability[24,25]) is used to calibrate the distance measurement results of the dual-interferometer system.

For the light coming out of the emitting collimator, the light field can be expressed as

$$E = E_0 e^{j(\omega t+\varphi_0)}, \tag{1}$$

where ω is the laser frequency, φ_0 is the initial phase of the light, and E_0 is the amplitude of the optical field. The optical fields of the first reference light and the measured light at receiving collimator 1 are

$$E_r = \frac{1}{2} E_0 \sqrt{R} e^{j(\omega t+\varphi_0+\varphi_1)}, \tag{2}$$

$$E_s = \frac{1}{4} E_0 \sqrt{R} e^{j(\omega t+\varphi_0+\varphi_1')}, \tag{3}$$

where E_r is the light field of the reference light and E_s is the light field of the measured light, assuming that the reflectivity of all mirrors is R. φ_1 and φ_1' are the phase changes produced by the reference light and the measured light passing through different optical paths, respectively. These two beams interfere at receiver collimator 1, and the intensity of the interference light received by PD1 is

$$I_1 = (E_r + E_s)(E_r + E_s)^* = \frac{5}{16} E_0^2 R + \frac{1}{4} E_0^2 R \cos(\varphi_1' - \varphi_1), \tag{4}$$

where $\varphi_1' - \varphi_1$ is the phase difference $\Delta\varphi_1$ between the first reference light and the measured light. Similarly, the intensity of the interference light received by PD2 can be obtained as

$$I_2 = \frac{1}{4} E_0^2 R + \frac{1}{4} E_0^2 R \cos(\varphi_2' - \varphi_2), \tag{5}$$

where $\varphi_2' - \varphi_2$ is the phase difference $\Delta\varphi_2$ between the second reference light and the measured light. ΔL_1 and ΔL_2 are the optical path differences between the reference light and the

measured light that interfere at receiver collimators 1 and 2, respectively. The relationship between (ΔL_1, ΔL_2) and ($\Delta\varphi_1$, $\Delta\varphi_2$) is

$$\Delta\varphi_1 = \frac{4\pi\Delta L_1}{\lambda}, \tag{6}$$

$$\Delta\varphi_2 = \frac{4\pi\Delta L_2}{\lambda}. \tag{7}$$

By adjusting the position of reference mirror 2 so that the difference between ΔL_1 and ΔL_2 is $\lambda/8 + N\lambda/2, N = 0, 1, 2, 3, \ldots,$

$$|\Delta L_1 - \Delta L_2| = \frac{\lambda}{8} + N\frac{\lambda}{2}. \tag{8}$$

Assuming that the target mirror is at a certain position A, Eqs. (6) and (7) are substituted into Eqs. (4) and (5), respectively, and the interference light intensities I_1 and I_2 at position A can be simplified by DC offset correction and normalizing the magnitude as follows:

$$I_{A_1} = \cos\frac{4\pi\Delta L_1}{\lambda}, \tag{9}$$

$$I_{A_2} = \cos\frac{4\pi\Delta L_2}{\lambda}. \tag{10}$$

Assuming $\Delta L_1 > \Delta L_2$, substituting Eq. (8) into Eq. (9) yields

$$I_{A_1} = \cos\left(\frac{4\pi\Delta L_2}{\lambda} + \frac{\pi}{2} + 2N\pi\right) = \sin\frac{4\pi\Delta L_2}{\lambda}. \tag{11}$$

Comparing Eqs. (10) and (11), it can be seen that when the target mirror is at a certain position, the interferometric light intensity output from the two detectors varies orthogonally.

Similarly, when the target mirror is moved Δx from position A to position B, the two interfering light intensities at position B can be simplified as

$$I_{B_1} = \sin\frac{4\pi(\Delta L_2 + 2\Delta x)}{\lambda}, \tag{12}$$

$$I_{B_2} = \cos\frac{4\pi(\Delta L_2 + 2\Delta x)}{\lambda}. \tag{13}$$

A schematic representation of the orthogonal detection method is shown in Fig. 2. When the target reflector is displaced, the output current is corrected for DC offset, and the amplitude is normalized to obtain blue and red lines that vary orthogonally, as shown in Fig. 2(a).

Using Eqs. (10) and (11), the phase ϕ_A is demodulated when the target mirror is located at position A,

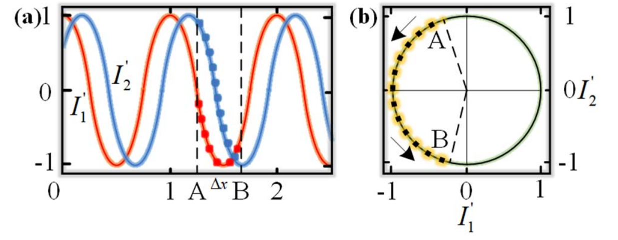

Fig. 2. (a) Two quadrature signals generated; (b) Lissajous graph.

$$\phi_A = \arccos\left(\frac{I_{A_1}}{\sqrt{I_{A_1}^2 + I_{A_2}^2}}\right). \tag{14}$$

Similarly, the phase ϕ_B is

$$\phi_B = \arccos\left(\frac{I_{B_1}}{\sqrt{I_{B_1}^2 + I_{B_2}^2}}\right). \tag{15}$$

Using Eqs. (14) and (15), we obtain the displacement

$$\Delta x = \frac{\lambda}{8\pi}\left|\arccos\left(\frac{I_{B_1}}{\sqrt{I_{B_1}^2 + I_{B_2}^2}}\right) - \arccos\left(\frac{I_{A_1}}{\sqrt{I_{A_1}^2 + I_{A_2}^2}}\right)\right|. \tag{16}$$

Assuming that all the noise introduced by the system is transformed into intensity noise with a coefficient of α, the light intensity of the two interferometric signals can be expressed as

$$I'_{A_1} = (1 + \alpha)I_{A_1}, \tag{17}$$

$$I'_{A_2} = (1 + \alpha)I_{A_2}. \tag{18}$$

Evidently, by substituting Eqs. (17) and (18) into Eqs. (14), the phase can still be demodulated. The effect of the noise on the interferometric system can be effectively eliminated using the orthogonal detection and inverse cosine demodulation algorithms.

The direction of the displacement can also be determined by measuring the two interferometric signals while measuring the displacement. In Fig. 2(b), the normalized interferometric signals I_1' and I_2' are represented on the x and y axes of the Lissajous graph, respectively. When the target mirror moves along the $x/-x$ motion direction, the points in the Lissajous graph move counterclockwise/clockwise along the circular path to determine the direction of movement. When the displacement Δx is equal to the laser wavelength, a complete circular path is achieved.

3. Experimental Results

3.1. Displacement direction discrimination

When the target mirror performs a sinusoidal vibration with a peak-to-peak value of 20 μm and a frequency of 5 Hz, the two

interference signals received by PD1 and PD2 are processed to obtain the mutually orthogonal sine/cosine curves, as shown in Figs. 3(a) and 3(b), respectively. When the target mirror moves along the x direction, the phase of the red line leads. When the target mirror moves along the $-x$ direction, the phase of the blue line leads, as shown in Fig. 3(c). The two interference signals before and after the change in the displacement direction were used to draw the Lissajous figure, as shown in Figs. 3(d) and 3(e). Due to the sinusoidal vibration of the target with a peak value of 20 μm (much greater than the wavelength of the laser of 1550 nm), the Lissajous figure appears as multiple complete circular paths. The direction of rotation of the points in the graph indicates the direction of motion of the object.

3.2. Nanometer-scale displacement measurement results

For comparison with the ranging results of the traditional interferometer, only the NPBS1, reference mirror 1, target mirror, and receiving collimator 1 were used to form the traditional interferometer. The target mirror moved 20 nm every 200 ms for 18 times. The traditional interferometer only provides an output interference signal I_1. The waveform of the processes signal is represented by the blue line in Fig. 4(a). The data for each 200 ms interval were averaged to obtain the yellow points in Fig. 4(a). The phase change $\Delta\varphi$ produced by each displacement is represented by the blue dots in Fig. 4(b). Evidently, at the extreme point of the interference cosine curve, the phase change produced by the 20 nm displacement is much smaller than the maximum slope of the cosine curve; that is, the ranging sensitivity changes with a change in displacement.

Consistent with the ranging conditions of a conventional interferometer, the orthogonal double interferometer adds an output signal. When the target moves, two mutually orthogonal interferometric signals are output by PD1 and PD2, as indicated by the red and blue lines in Fig. 4(c). The data were averaged every 200 ms to obtain the yellow line shown in Fig. 4(c). The phase change $\Delta\varphi$ produced by each displacement is obtained using Eqs. (14) and (15), as shown by the red dots in Fig. 4(b). Evidently, the phase change obtained by the orthogonal dual-interferometer system fluctuates around 10° during the 18 displacement measurements. It can be seen that the orthogonal type dual-interferometer system has better measurement consistency, which is relatively uniform and solves the disadvantage of the range sensitivity of the conventional interferometer system varying with displacement.

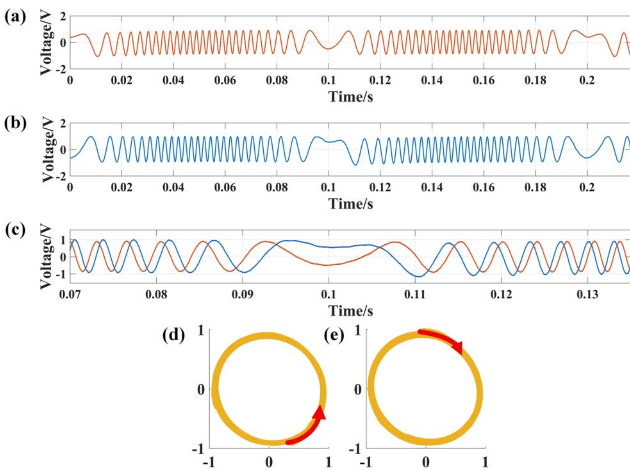

Fig. 3. (a) Interference signal received by PD1; (b) interference signal received by PD2; (c) interference signal variation diagram when the displacement direction is changed; (d) Lissajous figure when moving along the x direction; (e) Lissajous figure when moving along the $-x$ direction.

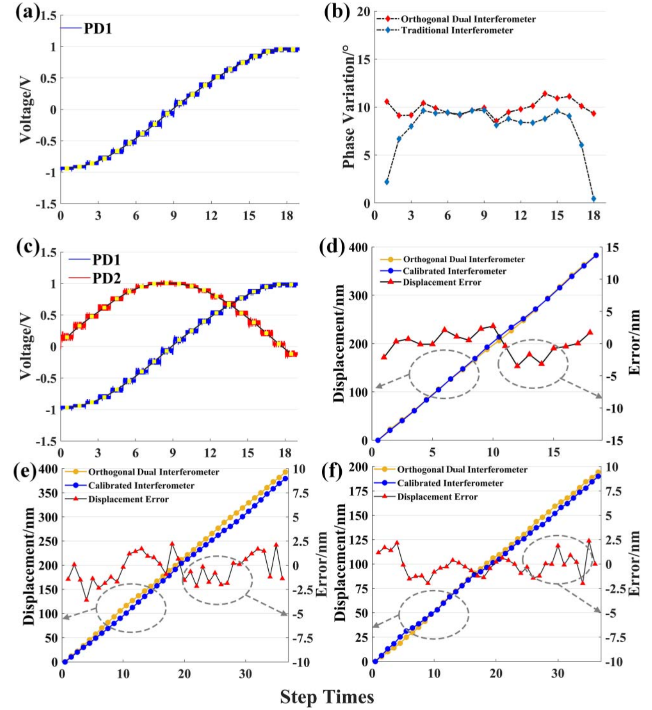

Fig. 4. (a) Conventional interferometer single-channel data acquisition; (b) phase difference resulting from each displacement; (c) orthogonal dual-interferometer two-way data acquisition; (d) 20 nm step displacement measurement results; (e) 10 nm step displacement measurement results; (f) 5 nm step displacement measurement results.

Substituting the phase change produced by each displacement into Eq. (16), the measured displacement of the dual-interferometer system is plotted, as indicated by the yellow points in Fig. 4(d). The measured displacement of the calibration interferometer is shown as the blue points in Fig. 4(d). Considering the measurement results of the calibration interferometer as a benchmark, the displacement error of the dual-interferometer system is plotted, as indicated by the red dots in Fig. 4(d). The experimental results show that, in the case of a displacement step of 20 nm, the dual-interferometer system using orthogonal detection has a high consistency with the measurement results of the calibration interferometer. The single measurement error fluctuates within ±5 nm. Subsequently, the limiting step of the orthogonal dual-interferometer system was explored.

Figures 4(e) and 4(f) show two sets of measurement results for the orthogonal dual interferometer and the calibration

Table 1. Orthogonal Dual-Interferometer Limit Resolution Error Results.

Step/nm	Number	Average Error/nm
20	36	0.29
10	36	0.27
5	36	0.12

interferometer with displacement steps of 10 and 5 nm, respectively. The blue points represent the measurement values of the calibration interferometer, the yellow points represent the measured displacement values of the orthogonal double interferometer system, and the displacement error curve is drawn as indicated by the red point. The displacement recovered using the orthogonal dual-interferometer system has a good linear relationship with the displacement measured by the calibration interferometer, and the errors of multiple measurements are basically within ±2.5 nm.

Table 1 lists the displacement measurement results for steps of 20, 10, and 5 nm. The average error increases with the increase of the displacement step. As shown in Fig. 5(a), owing to the installation error of the orthogonal dual interferometer and the calibration interferometer systems, it is shown that there is an angle θ between the measurement optical axis and the calibration optical axis. L is the measured displacement of the calibrated interferometer when the target moves from position 1 to position 2. $L \cos \theta$ is the measured displacement of the dual-interferometer system when the target moves from position 1 to position 2. When the displacement step size increases, the cosine error increases. Owing to changes in the environmental factors and device performance, the average error did not show a strict equal proportional increase.

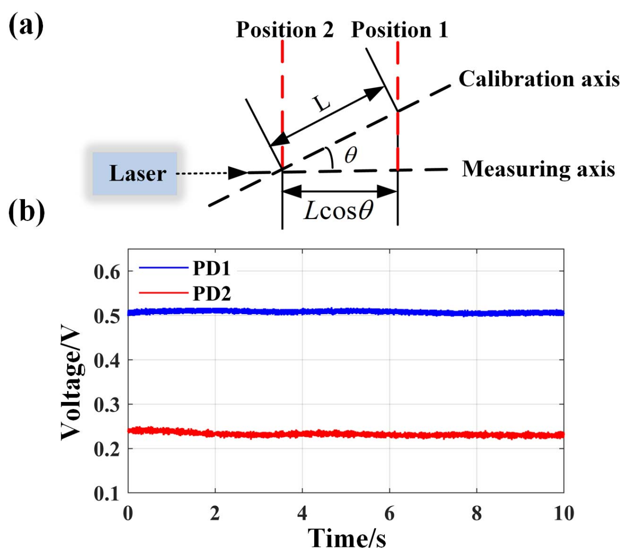

Fig. 5. (a) Schematic diagram of cosine error; (b) two interference signals when the target is stationary.

The system resolution is limited due to environmental fluctuations as well as system noise and other factors. Under the same experimental conditions, the two interferometric signals were acquired when the target reflector was stationary, as shown in Fig. 5(b). The phase fluctuation when the target is stationary can be demodulated using Eqs. (14) and (15), and the root mean square error of the phase at this time is calculated to obtain the fluctuation of the displacement, which is the system resolution. After acquisition and calculation, the range resolution of the dual-interferometer system was obtained as 700 pm.

The experimental results show that the developed double interferometer system has good repeatability for the measurement of nanoscale fine displacements and can be reliably used in the field of nanoscale displacement measurement.

4. Conclusion

A dual-interferometer high-precision microdisplacement measurement system using orthogonal demodulation was designed to solve the problems of uneven ranging sensitivity and the inability of the traditional interferometer to determine the displacement direction. The inverse cosine algorithm was used for displacement analysis. In the experiment, the minimum step length of the displacement system was measured as 5 nm. The experimental results exhibited a good linear relationship with the measurement results of the calibrated interferometer. The average error is 0.12 nm, and the repeatability is good. The experimental results show that the developed orthogonal double interferometer can realize a microdisplacement measurement of 5 nm with good repeatability, a simple system structure, and practical value.

Acknowledgement

This work was supported in part by the National Natural Science Foundation of China (No. 62005194).

References

1. H. Liang, Y. Sun, Z. Huang, C. Jiang, Z. Zhang, and L. Kan, "Reconstruction of fabry–perot cavity interferometer nanometer micro-displacement based on hilbert transform," Chin. Opt. Lett. **19**, 091202 (2021).
2. K. Kurokawa, S. Makita, Y.-J. Hong, and Y. Yasuno, "Two-dimensional micro-displacement measurement for laser coagulation using optical coherence tomography," Biomed Opt. Express **6**, 170 (2014).
3. S. Muñoz Solís, F. M. Santoyo, and M. del Socorro Hernández-Montes, "3D displacement measurements of the tympanic membrane with digital holographic interferometry," Opt. Express **20**, 5613 (2012).
4. Q. Wang, S. Yan, Q. Xu, S. Zhang, and L. Tu, "A universal high-sensitivity area-variation capacitive displacement transducer (CDT) based on fringe effect," IEEE Access **7**, 153650 (2019).
5. Y. Ye, C. Zhang, C. He, X. Wang, and J. Deng, "A review on applications of capacitive displacement sensing for capacitive proximity sensor," IEEE Access **8**, 45325 (2020).
6. S. Marick and S. C. Bera, "Study of a modified differential inductance type displacement transducer," in *International Conference on Electronics* (2014).

7. Y. Wu and T. Huang, "Design of high precision capacitance displacement sensor," in *IEEE Advanced Information Technology, Electronic and Automation Control Conference* (2018).
8. D. Guo, L. Shi, Y. Yu, X. Wei, and W. Ming, "Micro-displacement reconstruction using a laser self-mixing grating interferometer with multiple-diffraction," Opt. Express **25**, 31394 (2017).
9. M. Pisani, "Multiple reflection Michelson interferometer with picometer resolution," Opt. Express **16**, 21558 (2008).
10. J. N. Dash, R. Jha, J. Villatoro, and S. Dass, "Nano-displacement sensor based on photonic crystal fiber modal interferometer," Opt. Lett. **40**, 467 (2015).
11. K. Tian, J. Yu, X. Wang, H. Zhao, D. Liu, E. Lewis, G. Farrell, and P. Wang, "Miniature Fabry-Perot interferometer based on a movable microsphere reflector," Opt. Lett. **45**, 787 (2020).
12. E. Olivier and E. Janine, "Naked eye picometer resolution in a Michelson interferometer using conjugated twisted beams," Opt. Lett. **42**, 354 (2017).
13. W. Ye, M. Zhang, Y. Zhu, L. Wang, and C. Hu, "Tanslational displacement computational algorithm of the grating interferometer without geometric error for the wafer stage in a photolithography scanner," Opt. Express **26**, 34734 (2018).
14. Y. Yin, Z. Liu, S. Jiang, W. Wang, H. Yu, W. Li, and Jirigalantu, "Grating-based 2D displacement measurement with quadruple optical subdivision of a single incident beam," Opt. Express **29**, 24169 (2021).
15. M. Li, X. Xiang, C. Zhou, C. Wei, W. Jia, C. Xiang, Y. Lu, and S. Zhu, "Two-dimensional grating fabrication based on ultra-precision laser direct writing system," Acta Optica Sinica **39**, 0905001 (2019).
16. X. Chu, H. Lu, and J. Cao, "Research on direction recognizing and subdividing method for moiré (interference) fringes," Chin. Opt. Lett. **1**, 692 (2003).
17. X. Suan, C. Luc, and T. Suat, "Phase control of ellipsometric interferometer for nanometric positioning system," Sci. China Inf. Sci. **54**, 3424 (2011).
18. S. Xu, L. Chassagne, S. Topcu, L. Chen, J. Sun, and T. Yan, "Polarimetric interferometer for measuring nonlinearity error of heterodyne interferometric displacement system," Chin. Opt. Lett. **11**, 061201 (2013).
19. M. Zhu, H. Wei, S. Zhao, X. Wu, and Y. Li, "Subnanometer absolute displacement measurement using a frequency comb referenced dual resonance tracking Fabry–Perot interferometer," Appl. Opt. **54**, 4594 (2015).
20. B. Qi, D. E. Winder, and Y. Liu, "Quadrature phase-shifted optical demodulator for low-coherence fiber-optic Fabry-Perot interferometric sensors," Opt. Express **27**, 7319 (2019).
21. H. Fu, J. Tan, P. Hu, and Z. Fan, "Beam combination setup for dual-frequency laser with orthogonal linear polarization," Chin. Opt. Lett. **13**, 101201 (2015).
22. Z. Zhang, C. Jiang, F. Wang, Z. Huang, and C. Li, "Quadrature phase detection based on an extrinsic Fabry-Pérot interferometer for vibration measurement," Opt. Express **28**, 32572 (2020).
23. J. Cui, Z. He, Y. Jiu, J. Tan, and T. Sun, "Homodyne laser interferometer involving minimal quadrature phase error to obtain subnanometer nonlinearity," Appl. Opt. **55**, 7086 (2016).
24. T. Trottenberg and H. Kersten, "Measurement of forces exerted by low-temperature plasmas on a plane surface," Plasma Sources Sci. Technol. **26**, 055011 (2017).
25. M. Serra-Garcia, V. Peri, R. Susstrunk, O. R. Bilal, T. Larsen, L. G. Villanueva, and S. D. Huber, "Observation of a phononic quadrupole topological insulator," Nature **555**, 342 (2018).